

# Enhanced Electrochemical Stability of Sulfide-Based $\text{LiNi}_{0.8}\text{Mn}_{0.1}\text{Co}_{0.1}\text{O}_2$ All-Solid-State Batteries by Ti Surface Doping

Qing Zhang,<sup>[a]</sup> Andrea M. Bruck,<sup>[b]</sup> Alyssa M. Stavola,<sup>[b]</sup> Wentao Liang,<sup>[a]</sup> Peter Aurora,<sup>[a]</sup> and Joshua W. Gallaway<sup>\*[b]</sup>

All-solid-state batteries (ASSBs) using inorganic superionic conductors are considered a safer alternative to the current lithium ion battery technology. And tackling the issue of interfacial stability between the solid-state electrolyte and electrode active material is a critical step to achieving sustainable ASSBs. In this work, we applied a  $\text{TiO}_2$  surface coating on  $\text{LiNi}_{0.8}\text{Mn}_{0.1}\text{Co}_{0.1}\text{O}_2$  (NMC811) particles through a dry-coating process, and subsequently heat-treated the  $\text{TiO}_2$ -coated materials. We systematically characterized the changes to the material after the coating and heating processes, and we

explored the role of  $\text{TiO}_2$  coating and heat-treatment on the electrochemical cycling of NMC811 in a sulfide-based ASSB. The coating and heat treatment resulted in Ti doped into the NMC811 surface, which reduced undesired side reactions and improved cycling stability. Capacity retention of the doped material was 55% at 50 cycles, versus 11% in the un-doped material. The observations in this study provide an alternative approach toward enhancing the interfacial stabilities between high-energy NMC materials and sulfide-based solid-state electrolyte.

## 1. Introduction

Solidifying battery electrolytes is the most promising solution to address the safety concerns raised by the flammability of the liquid electrolytes with organic solvents in current lithium ion batteries. Extensive research efforts have been devoted to developing superionic solid-state electrolytes and pairing them with electrode materials to construct solid-state batteries. Among major classes of solid-state electrolyte materials, the sulfide family has demonstrated the highest Li-ion conductivity so far, up to  $25 \text{ mS}\cdot\text{cm}^{-1}$  at room temperature, because of the high polarizability of sulfur atoms.<sup>[1]</sup> And compared to oxide solid ion conductors, sulfide materials are more deformable at room temperature, enabling more efficient processing of high-energy bulk-type ASSBs. In spite of the appealing ion conductivity and processability, critical challenges such as poor air stability and high interfacial resistance with active electrode materials are hindering the practical application of sulfide-based electrolytes.<sup>[2-4]</sup> Characterization of the interface formed between sulfide electrolyte and three different active materials ( $\text{LiCoO}_2$ ,  $\text{LiNi}_{1/3}\text{Co}_{1/3}\text{Mn}_{1/3}\text{O}_2$  and  $\text{LiMn}_2\text{O}_4$ ) in the composite cathode demonstrated that sulfide can be oxidized into elemental sulfur, lithium polysulfide, phosphorus sulfide species and phosphates when they are in contact with transition metal oxide materials.<sup>[3,5]</sup> In addition to the structural disorder caused

by chemical instability, a space-charge layer formed at the interface can lead to depletion of Li ions on the sulfide side, lowering Li-ion conductivity.<sup>[6]</sup> Large interfacial resistance is developed as a result of these combined mechanisms, and significantly deteriorates the durability of the battery.<sup>[3,5]</sup>

Applying a layer of coating materials to the interfaces between solid electrolytes and cathode active materials has been demonstrated to effectively reduce undesirable electrode-electrolyte side reactions. To date, a number of oxide materials such as  $\text{LiNbO}_3$ ,<sup>[7]</sup>  $\text{Li}_4\text{Ti}_5\text{O}_{12}$ ,<sup>[8,9]</sup>  $\text{Li}_2\text{SiO}_3$ ,<sup>[8,10]</sup>  $\text{Li}_2\text{CO}_3\text{-Li}_2\text{BO}_3$ ,<sup>[11]</sup>  $\text{ZrO}_2$ ,<sup>[12]</sup> and  $\text{Al}_2\text{O}_3$ ,<sup>[13]</sup> have been applied on cathode active materials by wet-chemical approaches and the coated materials demonstrated enhanced interfacial stability in sulfide-based ASSBs. Based on first principle calculations, these coating materials are electrochemically stable and can achieve equilibrium chemical potential of Li with both the solid electrolyte and active material, stabilizing the interface.<sup>[14]</sup> The coating can also effectively suppress the growth of the space-charge layer and reduce the inhomogeneity of Li distribution.<sup>[6]</sup> Experimentally, Ohta et al. has proved that  $\text{LiNbO}_3$  coating can significantly improve the functional capacity by lowering the interfacial resistance. The optimum coating thickness was found to be between 8–12 nm. Li-In/ $\text{LiCoO}_2$  cells with  $\text{Li}_{3.25}\text{Ge}_{0.25}\text{P}_{0.75}\text{S}_4$  electrolyte using  $\text{LiNbO}_3$  coated  $\text{LiCoO}_2$  retained 74% of the original capacity when the current increased from  $0.13$  to  $5 \text{ mA}\cdot\text{cm}^{-2}$ , while only 7% of the capacity was retained for cell using bare  $\text{LiCoO}_2$ .<sup>[7]</sup> In another example, Machida et al. coated  $\text{ZrO}_2$  on  $\text{LiNi}_{1/3}\text{Mn}_{1/3}\text{Co}_{1/3}\text{O}_2$  (NMC111) by a sol-gel approach, and built  $\text{Li}_{4.4}\text{Si-NMC111}$  battery using  $\text{Li}_3\text{PS}_4$  electrolyte. The cell with 0.7 mol.%  $\text{ZrO}_2$ -coated NMC111 showed a higher initial discharge capacity of  $120 \text{ mAh}\cdot\text{g}^{-1}$ , and no capacity fade over 50 cycles. In comparison, the cell with bare NMC111 showed an initial discharge capacity of  $105 \text{ mAh}\cdot\text{g}^{-1}$ .

[a] Dr. Q. Zhang, Dr. W. Liang, Dr. P. Aurora  
Kostas Research Institute at Northeastern University  
Burlington, MA 01803, USA  
[b] Dr. A. M. Bruck, A. M. Stavola, Prof. J. W. Gallaway  
Department of Chemical Engineering  
Northeastern University  
Boston, MA 02115, USA  
E-mail: j.gallaway@northeastern.edu

and about 70 mAh·g<sup>-1</sup> was retained at 50<sup>th</sup> cycle. Corresponding impedance measurements suggested that without ZrO<sub>2</sub> coating, much more interfacial resistance increases as cycling progresses.<sup>[12]</sup>

Titanium oxides have been used as a coating on NMC materials to alleviate surface degradation and improve cycle life in batteries with liquid electrolyte with organic solvents.<sup>[15–17]</sup> And the cycling and characterization results have shown that a uniform TiO<sub>2</sub> coating could reduce electrode-electrolyte side reactions, and impede the formation of an insulating phase of NiO. While these TiO<sub>2</sub> coatings were mainly prepared by wet-chemical approaches, dry coating is a more cost-effective approach to coat material of larger particle size with smaller particles by mechanical milling, and has been used for battery active materials.<sup>[18,19]</sup> For example, a uniform MgO coating on LiCoO<sub>2</sub> prepared by ball milling significantly improved capacity retention. Moreover, the same study has shown that high temperature annealing of the coated material influenced doping levels of Mg ions and promoted better coating dispersion.<sup>[20]</sup>

In this work, surface and structural modifications of LiNi<sub>0.8</sub>Mn<sub>0.1</sub>Co<sub>0.1</sub>O<sub>2</sub> (NMC811) was achieved through a dry-coating followed by annealing process, where TiO<sub>2</sub> was successfully coated on NMC811 by high-energy ball milling, and the coated material was heat-treated. By coating TiO<sub>2</sub>, the cycling stability of NMC811 was improved, and heat-treating further significantly enhanced functional capacity and retention. The crystalline structures, morphology and microstructure, and chemical state of the raw and modified NMC materials were investigated to understand the underlying mechanisms. It was found that Ti was doped into the outer surface of NMC811 particles, and this provided improved stability in contact with Li<sub>6</sub>PS<sub>5</sub>Cl electrolyte during cycling.

## Experimental Section

### Preparation of materials

Crystalline solid electrolyte Li<sub>6</sub>PS<sub>5</sub>Cl was prepared by a solid-state approach. Starting materials Li<sub>2</sub>S (Alfa Aesar), P<sub>2</sub>S<sub>5</sub> (Alfa Aesar) and LiCl (anhydrous, Alfa Aesar) at a stoichiometric ratio were milled at 500 rpm for 10 hours in a planetary ball mill. Then the milled precursor was annealed at 550 °C for 5 hours to obtain the final electrolyte product. All the synthesis processes were carried out under inert atmosphere. LiNi<sub>0.8</sub>Mn<sub>0.1</sub>Co<sub>0.1</sub>O<sub>2</sub> (MSE Materials & Supplies) was used as received, and the untreated material is designated as NMC in the following text. The dry coating process was conducted by milling TiO<sub>2</sub> (anatase, Alfa Aesar, 325 mesh) and NMC at a weight ratio of 1:99 in a planetary ball mill, and the obtained product at this stage, TiO<sub>2</sub>-NMC, is designated as TNMC. Further, TNMC was heat-treated at 725 °C for 6 hours under oxygen to obtain the heat-treated TiO<sub>2</sub>-NMC material which is designated as HTNMC.

### Characterizations

Powder x-ray diffraction of the as-prepared NMC samples were performed on a Rigaku Ultima IV diffractometer using Cu K $\alpha$  radiation ( $\lambda = 1.54 \text{ \AA}$ ). Rietveld refinement of the observed diffrac-

tion patterns were conducted using GSAS-II.<sup>[21]</sup> Scanning electron microscopy (SEM) was performed on a FEI Scios Dualbeam system. Scanning/transmission electron microscopy (S/TEM) and energy dispersive X-ray spectroscopy (EDS) characterizations were performed on a probe-corrected FEI Titan Themis 300 scanning/transmission electron microscope with ChemiSTEM technology. All S/TEM and EDS images were collected at 300 kV. XPS measurement was conducted on a Thermo Fisher Nexa XPS instrument.

### Assembly and electrochemical test of all-solid-state batteries

Electrochemical performance of ASSBs was evaluated in a pressurized cell format, similar to previously reported bulk-type ASSBs,<sup>[22]</sup> with a 10 mm diameter electrode circle size. All ASSBs were assembled and tested in an argon-filled glovebox. The working electrode consisted of active material (NMC, TNMC or HTNMC) and solid-state electrolyte Li<sub>6</sub>PS<sub>5</sub>Cl in a weight ratio of 70:30. The areal loading of active material was 8.86 mg/cm<sup>2</sup>. Li<sub>6</sub>PS<sub>5</sub>Cl was used as solid electrolyte and separator. Indium metal served as the counter electrode. To assemble a solid-state cell, the cathode composite layer and solid electrolyte layer were pressed together uniaxially at 300 MPa. Indium metal was then attached to the opposite side of the electrolyte to the cathode, and the cell was pressed at 100 MPa. A metal fixture was used to maintain the cell pressure during cell cycling. An Arbin battery tester was used for galvanostatic tests. Cells were cycled in the voltage range of 2.0–3.7 V vs. Li–In (corresponding to 2.6–4.3 V vs. Li/Li<sup>+</sup>) at 0.1 C at room temperature. The potential of Li–In alloy is 0.6 V vs Li/Li<sup>+</sup>.<sup>[23]</sup> A constant voltage charging step was added to the end of charge process at 3.7 V vs Li–In (equals 4.3 V vs. Li) to ensure more complete de-lithiation of cathode material. Potential was limited to 4.3 V vs. Li to avoid Ni oxidation and conversion to NiO.

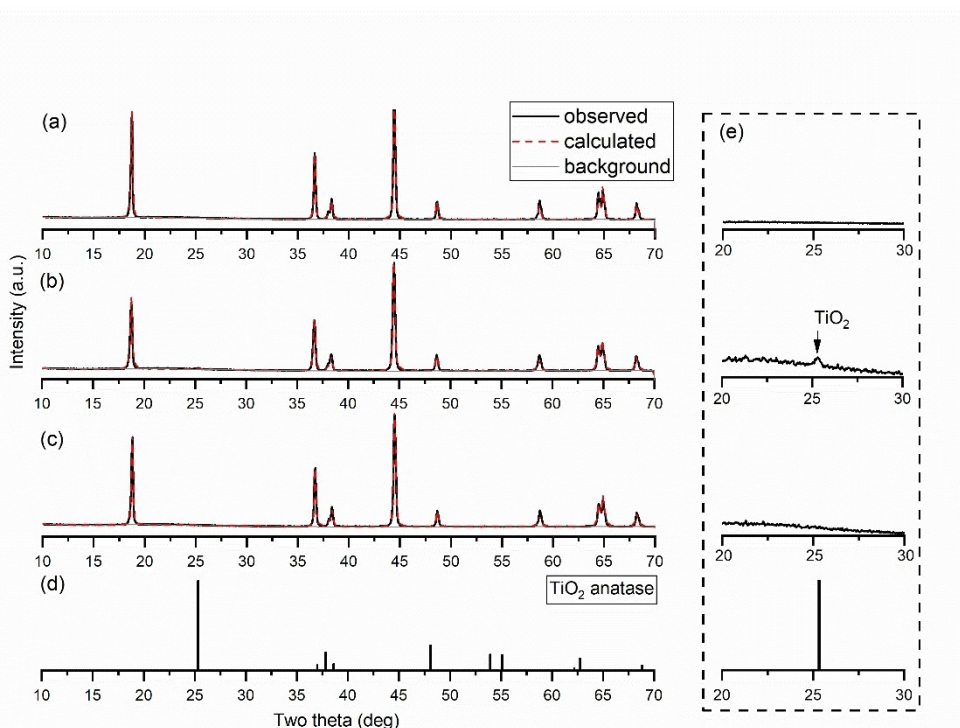
## 2. Results and Discussion

XRD patterns of NMC, TNMC and HTNMC are compared in Figure 1(a–c). There are no apparent peak shifts after the coating process. Noticeably, the (101) peak of TiO<sub>2</sub> anatase phase at 2 $\theta$  of 25° can be seen in the TNMC sample, as shown in the Figure 1(e), indicating that TiO<sub>2</sub> was introduced as a secondary phase. However, no additional diffraction peaks other than NMC are present in HTNMC, suggesting that TiO<sub>2</sub> was incorporated into the structure of NMC during the heat-treatment process.

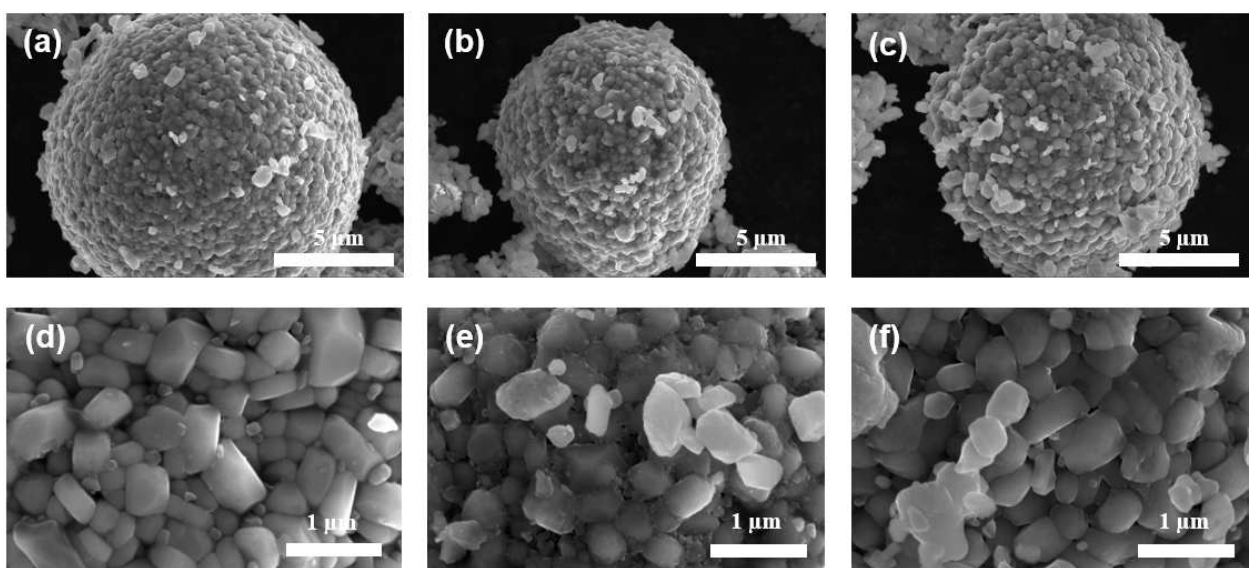
Each NMC material was analyzed using Rietveld refinement to identify any evidence of Ti<sup>4+</sup> doping and the structural variation accompanying the addition of TiO<sub>2</sub> and heat treatment. Table 1 summarizes the refinement results. In all samples, the NMC had a NaFeO<sub>2</sub>-type structure with an *R*-3*m* space group where the Ni, Mn and Co fractions were constrained to the stoichiometric ratios and only the Ni was allowed to mix

Table 1. Rietveld refinement results of NMC, TNMC, and HTNMC

	A [Å]	c [Å]	Volume [Å <sup>3</sup> ]	Li/Ni mixing [%]	TiO <sub>2</sub> [wt %]	wR [%]
NMC	2.8725(1)	14.2076(5)	101.529(4)	4.6(3)	N/A	4.01
TNMC	2.8719(1)	14.1958(6)	101.403(4)	5.2(2)	0.9 +/-0.2	3.42
HTNMC	2.8738(1)	14.2091(4)	101.635(3)	4.8(2)	N/A	3.20



**Figure 1.** XRD data of a) NMC, b) TNMC and c) HTNMC with calculated data from Rietveld refinement. d)  $\text{TiO}_2$  anatase phase reference patterns.<sup>[24]</sup> e) Expansion on the two-theta range from 20 to 30 degree region of (a–c).



**Figure 2.** SEM images of NMC samples. a) NMC, b) TNMC and c) HTNMC were taken at lower magnification. d) NMC, e) TNMC and f) HTNMC were taken at higher magnification.

into the Li interlayer due to the similar ionic radii of  $\text{Li}^+$  and  $\text{Ni}^{2+}$ , which has been previously described.<sup>[25]</sup> In TNMC, which contains anatase  $\text{TiO}_2$ , an additional  $I4_1/\text{amd}$  space group was used with no further modifications. Previously, it was found that  $\text{Ti}^{4+}$  substitution would increase the volume of the crystal lattice even at low doping levels of  $<2\%$ \* due to the larger octahedra size of the  $\text{Ti}^{4+}$  oxide ( $r=0.60 \text{ \AA}$ ) compared to the

other  $\text{M}^{3+}$  cations ( $\text{M}=\text{Ni, Co or Mn}$ ) which have a radius between  $0.56\text{--}0.53 \text{ \AA}$ .<sup>[26,27]</sup> The TNMC sample did not expand in volume compared to the NMC and shows a small decrease in volume with anatase peaks identified in the NMC pattern that were refined to a total  $0.9\text{--}0.2 \text{ wt\%}$   $\text{TiO}_2$ . This anatase phase could clearly be identified in the diffraction pattern and provides clear evidence that most  $\text{Ti}^{4+}$  remained in  $\text{TiO}_2$ .

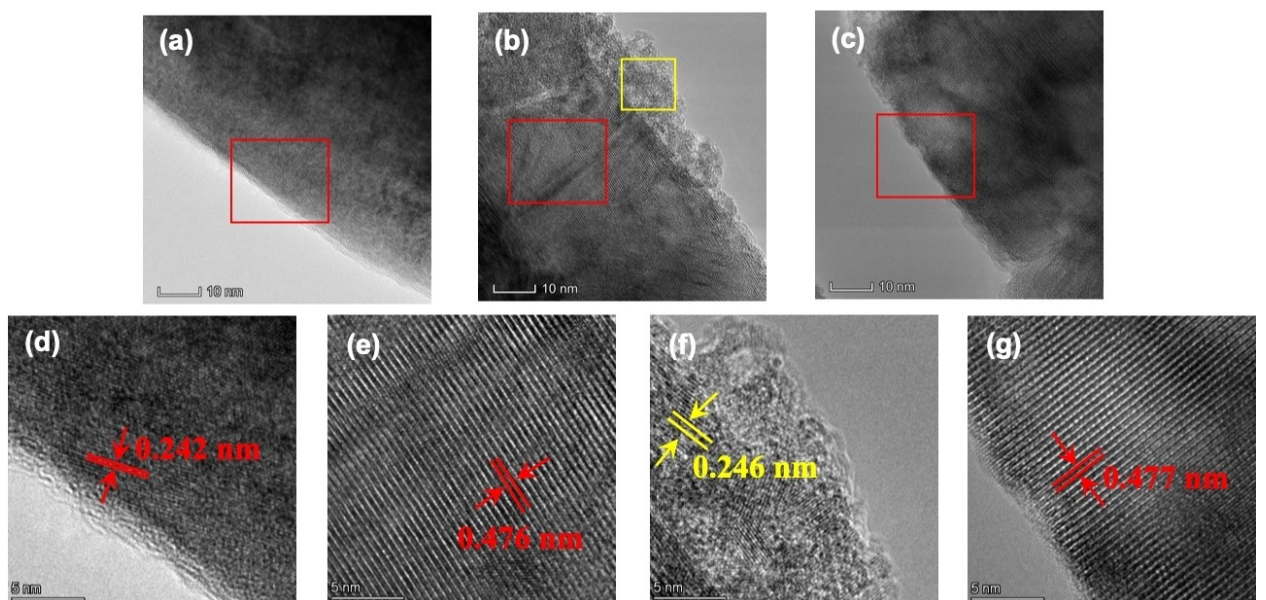


Figure 3. HRTEM images of a) NMC, b) TNMC and c) HTNMC. (d-g) are expanded images. d) corresponds to the red box region in (a); e) and f) corresponds to the red and yellow box region in (b), respectively; g) corresponds to the red box region in (c).

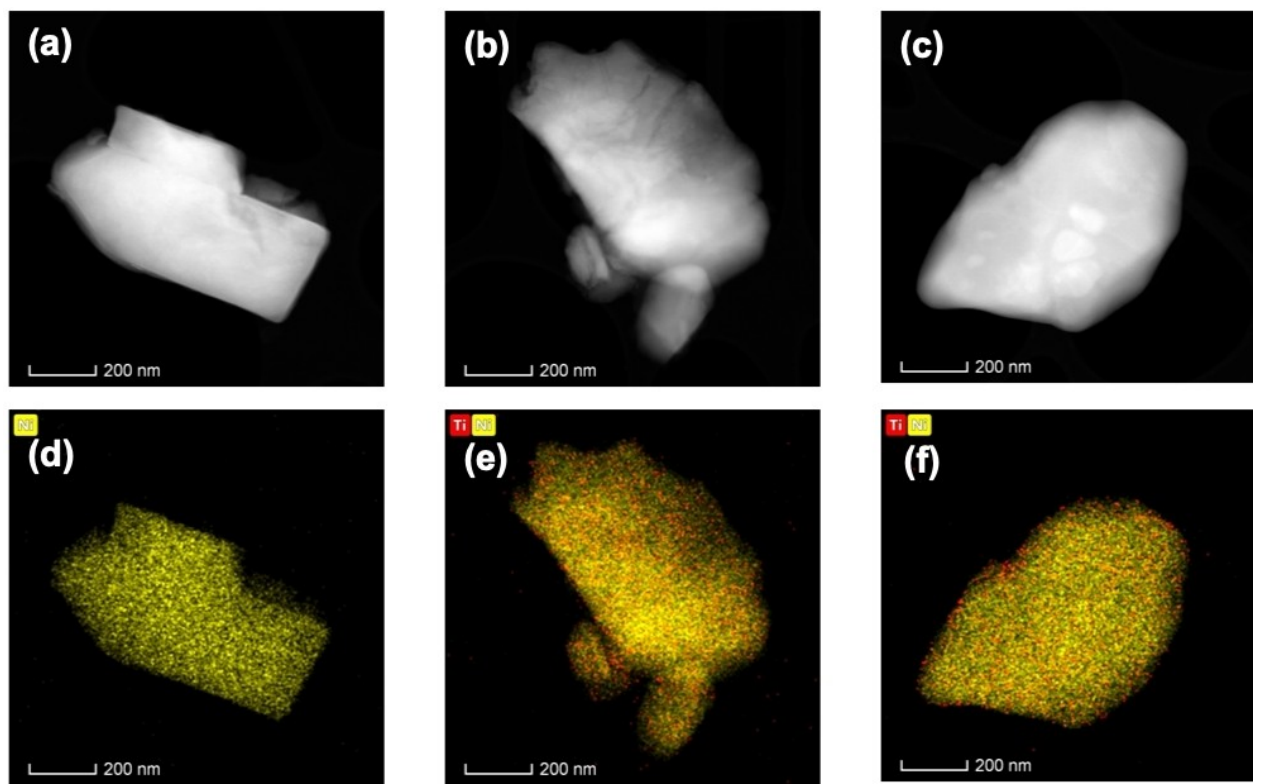


Figure 4. STEM images of a) NMC, b) TNMC and c) HTNMC. EDS elemental mapping of Ni and Ti of d) NMC, e) TNMC and f) HTNMC.

However, with the HTNMC material that went through a high temperature re-crystallization process, a small volume increase ( $+0.106 \text{ \AA}^3$ ) consistent with previous investigations provided evidence of a small amount of incorporated  $\text{Ti}^{4+}$ .<sup>[26,27]</sup> During the refinement the Ti corresponding to 1 wt%  $\text{TiO}_2$  was used for the model, providing good agreement between the

observed pattern as shown by Figure 1. Notice that throughout the refinements there is little variations in the Li/Ni mixing where this mixing corresponds to approximately 5% of the interlayer occupancy. Although previous investigations show  $\text{Ti}^{4+}$  can inhibit Li/Ni mixing the results from this investigation show no major variation between samples.<sup>[27]</sup>

The scanning electron microscope images of NMC, TNMC and HTNMC are shown in Figure 2. Typical spherical morphology was observed for all three samples. 5–10  $\mu\text{m}$  particles were formed by aggregation of 200–500 nm primary particles, Figure 2(a–c). The  $\text{TiO}_2$  material used in this study had a particle size of 100–200 nm. At higher magnification, TNMC clearly shows that the boundary of primary particles was more blurred, and particles are covered by another layer of material, indicating  $\text{TiO}_2$  particles were broken down during milling and a coating was successfully formed. However, HTNMC showed a similar surface structure to bare NMC. Particle boundary was clear and no surface coating was visible. The SEM observations suggested that single-phase material was likely formed after heat-treating, agreeing well with the XRD results.

The microstructure of particle surface is revealed by HRTEM images in Figure 3(a–c). For TNMC, a coating layer is clearly presented on the surface of the NMC core, and the thickness of the coatings ranges from 2–15 nm, Figure 3(b). The variation of thickness can be attributed to the morphology and surface structure of the NMC cores, but most of the surface is obviously coated. However, no surface coating is visible on the surface of HTNMC particle, Figure 3(c). Areas in the red and yellow boxes in Figure 3(a–c) are expanded in Figure 3(d–g) to analyze the lattice fringes. Interplanar spacing of NMC (Figure 3(d)), TNMC (Figure 3(e)) and HTNMC (Figure 3(g)) was measured to be

0.242, 0.476 and 0.477 nm, respectively, matching well with the (101), (003) and (003) plane, respectively. The d-spacing of the coating layer of the TNMC sample was measured to be 0.246 nm, matching well with  $\text{TiO}_2$  anatase (004) reflection, Figure 3(f).

STEM images in Figure 4(a–c) revealed that the primary particle size was about several hundred nanometers, in alignment with SEM data. And agreeing with HRTEM, both TNMC and HTNMC showed uniform distribution of Ti, based on EDS elemental mapping, Figure 4(d–f). These mapping results corroborated that TNMC had continuous coverage of  $\text{TiO}_2$  coating, and HTNMC most likely had Ti infiltrated into the structure and formed a single-phase material.

The cycling results of NMC, TNMC and HTNMC are compared in Figure 5. The sulfide electrolyte argyrodite-structure  $\text{Li}_2\text{PS}_5\text{Cl}$  used in the study had an Li ionic conductivity of  $1.6 \text{ mS}\cdot\text{cm}^{-1}$  at room temperature, in accordance with literature reports.<sup>[28,29]</sup> NMC, TNMC and HTNMC demonstrated an initial charge capacity of 187.2, 108.3 and  $176.5 \text{ mAh}\cdot\text{g}^{-1}$ , respectively, and an initial discharge capacity of 90.3, 52.5 and  $105.0 \text{ mAh}\cdot\text{g}^{-1}$ , respectively. The capacity loss on first charge is a combined factor of electrode-electrolyte side reactions due to the instability between the NMC and  $\text{Li}_2\text{PS}_5\text{Cl}$  electrolyte, and slow Li diffusion due to lattice distortion at higher lithiation state.<sup>[30]</sup> It has been proven elsewhere that  $\text{Ti}^{4+}$  provides extra

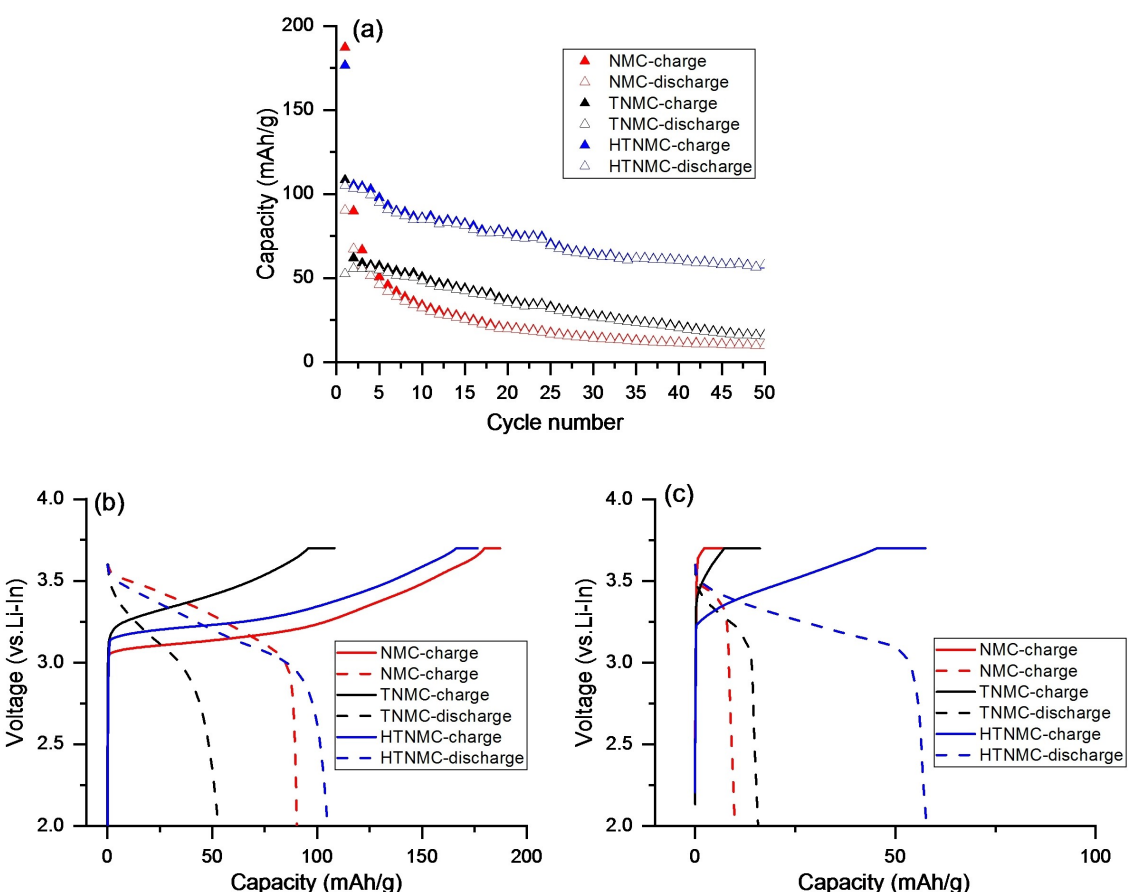


Figure 5. a) Cycling results of NMC, TNMC and HTNMC, and voltage profiles of b) the 1<sup>st</sup> cycle and c) the 50<sup>th</sup> cycle.

electrons and thus retards the oxidation of  $\text{Ni}^{3+}$  to  $\text{Ni}^{4+}$ , which accounts of the lower initial lithiation capacity of TNMC and HTNMC.<sup>[26,31]</sup> Moreover, the presence of ionically insulating  $\text{TiO}_2$  coating on TNMC induced higher surface resistance, consequently the initial lithiation capacity was further reduced. After 50 cycles, NMC, TNMC and HTNMC retained a discharge capacity of 9.9, 15.7 and 57.8 mAh·g<sup>-1</sup>, respectively, corresponding to a capacity retention of 11.0%, 29.9% and 55.0%, respectively. Despite the lower initial discharge capacity of TNMC compared to NMC, the following cycling proved higher capacity retention capability because the coating effectively impeded electrode-electrolyte side reactions. Further, based on the cycling results, HTNMC showed more advantageous cycling stability, indicating that Ti-infiltrated structure had higher interfacial stability and lower reactivity with the electrolyte material.

X-ray photoelectron spectroscopy measurements are shown in Figure 6, and were carried out to investigate the oxidation state of nickel on the surface of the three NMC materials. The Ni 2p core emission has two main parts, Ni 2p<sub>3/2</sub> peak at 854.5 eV and Ni 2p<sub>1/2</sub> peak at 872.1 eV, with associated satellite peaks located at 861.1 and 878 eV, respectively.<sup>[32,33]</sup> Two main components at ~854.5 eV and 855.5 eV are in accordance with  $\text{Ni}^{2+}$  and  $\text{Ni}^{3+}$  respectively. Based on fitting results, the relative ratio of  $\text{Ni}^{2+}/\text{Ni}^{3+}$  of the three samples are 0.23, 0.40 and 0.73 for NMC, TNMC and HTNMC, respectively. The theoretical  $\text{Ni}^{2+}/\text{Ni}^{3+}$  ratio of NMC811 is about 0.143.<sup>[34]</sup>  $\text{TiO}_2$  coating process led to the reduction of  $\text{Ni}^{3+}$  to  $\text{Ni}^{2+}$ , presumably this could be

related to  $\text{Ti}^{4+}$  substitution of  $\text{Ni}^{3+}$  due to similar ionic radii ( $\text{Ti}^{4+}$  0.0605 nm,  $\text{Ni}^{3+}$  0.056 nm,  $\text{Ni}^{2+}$  0.069 nm,  $\text{Co}^{3+}$  0.0545 nm and  $\text{Mn}^{4+}$  0.053 nm). Since major changes to the NMC structure were not seen in diffraction data and  $\text{TiO}_2$  remained a separate phase, the changes to chemical state are believed to occur only on the surface. The  $\text{Ni}^{2+}/\text{Ni}^{3+}$  ratio of HTNMC further increased, suggesting that more  $\text{Ni}^{3+}$  ions were substituted by  $\text{Ti}^{4+}$  during the annealing and re-crystallization process. The dissociation energy of Ti–O bond is much stronger than that of Ni–O, Co–O and Mn–O bond, which accounts for the lower reactivity with sulfides.<sup>[35]</sup> Considering the changes to the structure observed in diffraction where HTNMC is a single-phase material and has a bigger unit cell volume,  $\text{Ti}^{4+}$  infiltrated deeper into the bulk during annealing. However, limited by the penetration depth of XPS, the observed changes to the  $\text{Ni}^{2+}/\text{Ni}^{3+}$  ratio can only represent the surface of the material (in nanometer range). The changes to the chemical state and the substitution mechanisms in the bulk of the material cannot be concluded from XPS data. It is worth noting that despite a higher  $\text{Ni}^{2+}/\text{Ni}^{3+}$  ratio, the  $\text{Li}^+/\text{Ni}^{2+}$  cation mixing was not significantly increased for HTNMC and the material remained structurally stable. Further, for the TNMC and HTNMC material, the peak position of Ti 2p doublets, Ti 2p<sub>3/2</sub> (at 463.5 eV) and Ti 2p<sub>1/2</sub> (at 457.9 eV) remained unchanged after the heating process, and both materials showed the Ti was at +4 oxidation state.

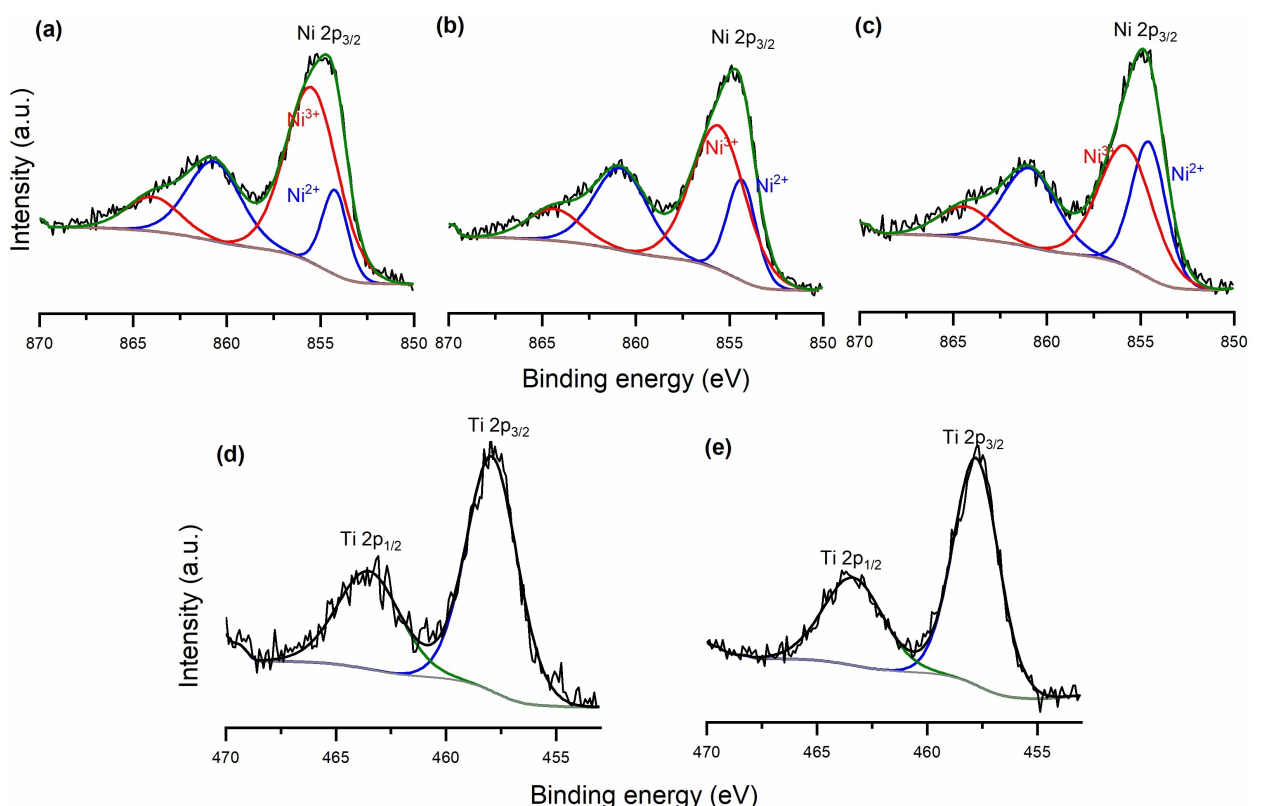


Figure 6. XPS of Ni 2p<sub>3/2</sub> spectra of a) NMC, b) TNMC and c) HTNMC. Ti 2p emission of d) TNMC and e) HTNMC.

### 3. Conclusions

In this study, to improve the compatibility of  $\text{LiNi}_{0.8}\text{Mn}_{0.1}\text{Co}_{0.1}\text{O}_2$  material with  $\text{Li}_2\text{PS}_5\text{Cl}$  solid-state electrolyte,  $\text{LiNi}_{0.8}\text{Mn}_{0.1}\text{Co}_{0.1}\text{O}_2$  material was coated with  $\text{TiO}_2$  through a dry-process, and the coated material was further annealed. The coated and subsequently annealed materials were systematically characterized, and results showed Ti infiltration into the NMC structure after annealing and led to reduction of  $\text{Ni}^{3+}$  to  $\text{Ni}^{2+}$ , likely due to substitution of  $\text{Ni}^{3+}$  by  $\text{Ti}^{4+}$ . The electrochemical cycling results have demonstrated the advantages of TNMC and HTNMC. While  $\text{TiO}_2$  coating can act as a physical barrier to impede electrode-electrolyte side reactions,  $\text{TiO}_2$  was insulating and results in lower functional capacity. The annealed HTNMC where Ti infiltrated into the NMC structure was superior in cycling stability as a result of the lower surface reactivity with sulfides. By inherently modifying structural properties of the material, the results in this study shed light on a new path toward improving the compatibility of NMC materials with sulfide-based electrolyte.

### Acknowledgements

This work was supported by the Office of Naval Research (Code 311) under OTA N000141890001. The authors thank Shawn Lafferty, Ted Rodill, and David Luzzi at the Kostas Research Institute for support. The authors thank Hongli Zhu at Northeastern University for invaluable assistance with the metal sulfide electrolyte. This work used resources from the XRD facility at Northeastern University Center for Renewable Energy Technology (NUCRET) and the TEM facility at Kostas Research Institute. The authors also thank Harvard University Center for Nanoscale Systems for the support on XPS. Distribution A: Approved for public release, distribution is unlimited. Document Control Number (DCN #): 43-6784-20.

### Conflict of Interest

The authors declare no conflict of interest.

**Keywords:** all-solid-state batteries • energy storage • metal sulfide electrolyte • NMC • Ti doping

- [1] Y. Kato, S. Hori, T. Saito, K. Suzuki, M. Hirayama, A. Mitsui, M. Yonemura, H. Iba, R. Kanno, *Nat. Energy.* **2016**, *1*, 16030.
- [2] A. Hayashi, H. Muramatsu, T. Ohtomo, S. Hama, M. Tatsumisago, *J. Alloys Compd.* **2014**, *591*, 247–250.
- [3] J. Auvergnat, A. Cassel, J.-B. Ledeuil, V. Viallet, V. Seznec, R. Dedryvère, *Chem. Mater.* **2017**, *29*, 3883–3890.

- [4] N. J. J. de Klerk, M. Wagemaker, *ACS Appl. Mater. Interfaces* **2018**, *1*, 5609–5618.
- [5] X. He, Y. Zhu, Y. Mo, *Nat. Commun.* **2017**, *8*, 15893.
- [6] J. Haruyama, K. Sodeyama, L. Han, K. Takada, Y. Tateyama, *Chem. Mater.* **2014**, *26*, 4248–4255.
- [7] N. Ohta, K. Takada, I. Sakaguchi, L. Zhang, R. Ma, K. Fukuda, M. Osada, T. Sasaki, *Electrochim. Commun.* **2007**, *9*, 1486–1490.
- [8] N. Ohta, K. Takada, L. Zhang, R. Ma, M. Osada, T. Sasaki, *Adv. Mater.* **2006**, *18*, 2226–2229.
- [9] H. Kitaura, A. Hayashi, K. Tadanaga, M. Tatsumisago, *Solid State Ionics* **2011**, *192*, 304–307.
- [10] A. Sakuda, A. Hayashi, M. Tatsumisago, *Chem. Mater.* **2010**, *22*, 949–956.
- [11] S. H. Jung, K. Oh, Y. J. Nam, D. Y. Oh, P. Brüner, K. Kang, Y. S. Jung, *Chem. Mater.* **2018**, *30*, 8190–8200.
- [12] N. Machida, J. Kashiwagi, M. Naito, T. Shigematsu, *Solid State Ionics* **2012**, *225*, 354–358.
- [13] J. H. Woo, J. J. Travis, S. M. George, S.-H. Lee, *J. Electrochem. Soc.* **2015**, *162*, A344–A349.
- [14] Y. Zhu, X. He, Y. Mo, *J. Mater. Chem. A* **2016**, *4*, 3253–3266.
- [15] W. Liu, M. Wang, X. I. Gao, W. Zhang, J. Chen, H. Zhou, X. Zhang, *J. Alloys Compd.* **2012**, *543*, 181–188.
- [16] Y. Cho, Y.-S. Lee, S.-A. Park, Y. Lee, J. Cho, *Electrochim. Acta* **2010**, *56*, 333–339.
- [17] J. M. Zheng, J. Li, Z. R. Zhang, X. J. Guo, Y. Yang, *Solid State Ionics* **2008**, *179*, 1794–1799.
- [18] Q. Zhou, L. Qu, T. Gengenbach, I. Larson, P. J. Stewart, D. A. V. Morton, *AAPS PharmSciTech.* **2013**, *14*, 38–44.
- [19] C. D. Kablitz, N. A. Urbanetz, *Pharm. Dev. Technol.* **2013**, *18*, 39–45.
- [20] J.-H. Shim, S. Lee, S. S. Park, *Chem. Mater.* **2014**, *26*, 2537–2543.
- [21] B. H. Toby, R. B. Von Dreele, *J. Appl. Crystallogr.* **2013**, *46*, 544–549.
- [22] R. Koerver, I. Aygün, T. Leichtweiß, C. Dietrich, W. Zhang, J. O. Binder, P. Hartmann, W. G. Zeier, J. Janek, *Chem. Mater.* **2017**, *29*, 5574–5582.
- [23] A. L. Santhosa, L. Medenbach, J. R. Buchheim, P. Adelhelm, *Batteries Supercaps.* **2019**, *2*, 524–529.
- [24] M. Horn, C. F. Schwerdtfeger, E. P. Meagher, *Z. Kristallogr. Cryst. Mater.* **1972**, *136*, 273–281.
- [25] S.-T. Myung, F. Maglia, K.-J. Park, C. S. Yoon, P. Lamp, S.-J. Kim, Y.-K. Sun, *ACS Energy Lett.* **2017**, *2*, 196–223.
- [26] Y. Mo, L. Guo, H. Jin, B. Du, B. Cao, Y. Chen, D. Li, Y. Chen, *J. Power Sources* **2020**, *448*, 227439.
- [27] Q.-Q. Qiu, Z. Shadik, Q.-C. Wang, X.-Y. Yue, X.-L. Li, S.-S. Yuan, F. Fang, X.-J. Wu, A. Hunt, I. Waluyo, S.-M. Bak, X.-Q. Yang, Y.-N. Zhou, *ACS Appl. Mater. Interfaces.* **2019**, *11*, 23213–23221.
- [28] C. Yu, L. van Eijck, S. Ganapathy, M. Wagemaker, *Electrochim. Acta* **2016**, *215*, 93–99.
- [29] S. Boulineau, M. Courty, J.-M. Tarascon, V. Viallet, *Solid State Ionics* **2012**, *221*, 1–5.
- [30] J.-M. Lim, T. Hwang, D. Kim, M.-S. Park, K. Cho, M. Cho, *Sci. Rep.* **2017**, *7*, 39669.
- [31] I. M. Markus, F. Lin, K. C. Kam, M. Asta, M. M. Doeff, *J. Phys. Chem. Lett.* **2014**, *5*, 3649–3655.
- [32] X. Yang, D. Wang, R. Yu, Y. Bai, H. Shu, L. Ge, H. Guo, Q. Wei, L. Liu, X. Wang, *J. Mater. Chem. A* **2014**, *2*, 3899–3911.
- [33] Y. Ding, B. Deng, H. Wang, X. Li, T. Chen, X. Yan, Q. Wan, M. Qu, G. Peng, *J. Alloys Compd.* **2019**, *774*, 451–460.
- [34] Z. Fu, J. Hu, W. Hu, S. Yang, Y. Luo, *Appl. Surf. Sci.* **2018**, *441*, 1048–1056.
- [35] Y. Chen, Y. Li, W. Li, G. Cao, S. Tang, Q. Su, S. Deng, J. Guo, *Electrochim. Acta* **2018**, *281*, 48–59.

Manuscript received: September 10, 2020  
 Revised manuscript received: November 11, 2020  
 Accepted manuscript online: December 3, 2020  
 Version of record online: December 17, 2020